

# Contact Binaries as Viable Distance Indicators: New, Competitive $(V)JHK_s$ Period–Luminosity Relations

Xiaodian Chen<sup>1,2</sup>, Richard de Grijs<sup>1,3</sup>, and Licai Deng<sup>2</sup>

## ABSTRACT

Based on the largest catalogs currently available, comprising 6090 contact binaries (CBs) and 2167 open clusters, we determine the near-infrared  $JHK_s$  CB period–luminosity (PL) relations, for the first time achieving the low levels of intrinsic scatter that make these relations viable as competitive distance calibrators. To firmly establish our distance calibration on the basis of open cluster CBs, we require that (i) the CB of interest must be located inside the core radius of its host cluster; (ii) the CB’s proper motion must be located within the  $2\sigma$  distribution of that of its host open cluster; and (iii) the CB’s age,  $t$ , must be comparable to that of its host cluster, i.e.,  $\Delta \log(t \text{ yr}^{-1}) < 0.3$ . We thus select a calibration sample of 66 CBs with either open cluster distances or accurate space-based parallaxes. The resulting near-infrared PL relations, for both late-type (i.e., W Ursae Majoris-type) and—for the first time—early-type CBs, are as accurate as the well-established  $JHK_s$  Cepheid PL relations, (characterized by single-band statistical uncertainties of  $\sigma < 0.10$  mag). We show that CBs can be used as viable distance tracers, yielding distances with uncertainties of better than 5% for 90% of the 6090 CBs in our full sample. By combining the full  $JHK_s$  photometric data set, CBs can trace distances with an accuracy,  $\sigma = 0.05$  (statistical)  $\pm 0.03$  (systematic) mag. The 102 CBs in the Large Magellanic Cloud are used to determine a distance modulus to the galaxy of  $(m - M_V)_0^{\text{LMC}} = 18.41 \pm 0.20$  mag.

*Subject headings:* binaries: eclipsing — open clusters and associations: general — stars: distances

---

<sup>1</sup>Kavli Institute for Astronomy & Astrophysics and Department of Astronomy, Peking University Yi He Yuan Lu 5, Hai Dian District, Beijing 100871, China; chenxiaodian1989@163.com, grijs@pku.edu.cn

<sup>2</sup>Key Laboratory for Optical Astronomy, National Astronomical Observatories, Chinese Academy of Sciences, 20A Datun Road, Chaoyang District, Beijing 100012, China

<sup>3</sup>International Space Science Institute–Beijing, 1 Nanertiao, Zhongguancun, Hai Dian District, Beijing 100190, China

## 1. Introduction

Contact binaries (CBs), i.e., binary systems where both stellar components overfill and transfer material through their Roche lobes, are common among the field stellar population. Their population density in the solar neighborhood and the Galactic bulge is approximately 0.2%, while in the Galactic disk it is, on average,  $\sim 0.1\%$  (Rucinski 2006). CBs are divided into early- and late-type systems; the latter are also known as W Ursae Majoris (W UMa) systems. It has been established observationally that the two binary components have similar temperatures but unequal masses, which is known as Kuiper’s paradox (Kuiper 1941). Therefore, Lucy (1968) proposed convective common-envelope evolution as the key idea of CB theory. The modern scenario is that CBs are formed through angular-momentum loss (AML; Stępień 2006; Yıldız & Doğan 2013).

Although CBs are some seven magnitudes fainter than Cepheid variables, within the same distance range their number is three orders of magnitude larger. Unlike Cepheids, however, which trace young ( $\lesssim 20$  Myr-old) features, CBs map 0.5–10 Gyr-old stellar populations. Although RR Lyrae stars also trace structures older than 1–2 Gyr, very few RR Lyrae have been found in either open clusters (OCs) or the solar neighborhood.

Since Eggen (1967)’s seminal work, these considerations have led to a number of attempts at using CB period–luminosity (PL)–color (PLC) relations as potential distance indicators. Rucinski (1994) obtained a (widely used) PLC relation based on 18 W UMa-type CBs. Rucinski & Duerbeck (1997) improved their PLC relation based on 40 W UMa-type CBs using *Hipparcos* parallaxes with an accuracy in the corresponding distance moduli of  $\epsilon_M < 0.5$  mag. Rucinski (2006) subsequently derived a CB luminosity function from the All Sky Automated Survey (ASAS) and explored the viability of a *V*-band PL relation. However, his PL relation exhibited only a weak correlation and was affected by large uncertainties.

Despite a large volume of new data, studies advocating W UMa-type CB PL relations as viable distance indicators have made little progress during the past decade. In addition to calibration inhomogeneities stemming from difficulties in dealing with extinction and the use of multiple studies based on a few objects at a time, the current impasse is predominantly caused by difficulties in distinguishing foreground and background CBs from genuine OC members. Since CBs represent old stellar populations, they need a comparably long formation timescale, so for a typical old OC with 500 stellar members, one or more of its CBs could be misidentified as a cluster member.<sup>1</sup> In denser environments, the potential contamination

---

<sup>1</sup>Support for this estimate is provided by Chen et al. (2016), who assessed stellar contamination in the low-density OC NGC 188. Of 910 stars detected in a  $20 \times 20$  arcmin<sup>2</sup> region centered on the cluster, 532 are

by field CBs is even more significant.

To address these difficulties conclusively, here we introduce a joined-up OC–CB analysis based on carefully considered proper-motion and age-selection criteria (Chen et al. 2015). We have collected the largest CB sample currently available. We thus obtain the first truly viable near-infrared (NIR) CB PL relations, which are comparably accurate as the well-established  $JHK_s$  Cepheid PL relations.

In Section 2, we summarize the theory underlying the CB PL relations. The method used to select OC CBs and obtain OC distances is discussed in Section 3. The resulting  $JHK_s$  and  $V$ -band PL relations, as well as the corresponding period–color relations, are explored in Section 4. We discuss CBs as distance tracers and determine the distance to the Large Magellanic Cloud (LMC) in Section 5, followed by a summary of our main conclusions in Section 6.

## 2. Theoretical framework

From the equations governing contact binaries,

$$\begin{aligned} G(m_1 + m_2) &= (2\pi/P)^2 A^3, \\ A &\equiv (R/R_\odot)/r, \\ L/L_\odot &= (T_{\text{eff}}/T_{\text{eff},\odot})^4 (R/R_\odot)^2, \text{ and} \\ M_{\text{bol}} &= M_V + \text{BC}, \end{aligned} \tag{1}$$

a relationship between the distance modulus and other physical parameters (expressed in solar units) follows trivially,

$$\begin{aligned} (V_{\text{max}} - M_V) &= -39.189 + V_{\text{max}} + \text{BC} + 10 \log T_1 + 5 \log r \\ &\quad + \frac{5}{3} \log m_1 + \frac{10}{3} \log P + \frac{5}{3} \log(1 + q), \end{aligned} \tag{2}$$

where  $V_{\text{max}}$ ,  $M_V$ , and  $M_{\text{bol}}$  are the maximum and absolute  $V$ -band magnitudes and the bolometric magnitude of the binary system, respectively, ‘BC’ is the bolometric correction,  $T_1, T_2, m_1$ , and  $m_2$  are the temperatures and masses of both components,  $q \equiv m_2/m_1$  is the system’s mass ratio,  $P$  its orbital period,  $A$  and  $R$  are the semi-major axis and the stellar radius (assuming blackbody radiation, which is an incorrect assumption for realistic stellar atmospheres but which has very little influence on our final results),  $r_1$  and  $r_2$  are the radii

---

cluster members, while one foreground CB was found among the 378 contaminants.

of both components in units of the semi-major axis, and the relative radius  $r$ , in the same units, is defined as

$$r = \left( r_1^2 + r_2^2 \left( \frac{T_2}{T_1} \right)^4 \right)^{\frac{1}{2}}. \quad (3)$$

Since  $m_1$  and  $q$  depend on the effective temperature,  $T_{\text{eff}}$ , Rucinski (1994) suggested that the terms,  $5 \log r + \frac{5}{3} \log(1+q) + \frac{5}{3} \log(m_1)$ , may be omitted. Indeed, for 100 well-studied CBs with known parameters (Yıldız & Doğan 2013), an obvious linear relationship is apparent between  $5 \log r + \frac{5}{3} \log(1+q) + \frac{5}{3} \log(m_1)$  and  $\log T_{\text{eff}}$ . Therefore, a simplified PLC relation is indeed well established, taking the form  $L = a \log P + b \log(T_{\text{eff}}) + \text{constant}$  (where  $a$  and  $b$  are constants). By reference to the Cepheid PLC and PL relations, W UMa-type CBs are thus expected to follow a PL relation if they also exhibit linear period–color or luminosity–color relations. Similarly as for Cepheids, the resulting CB PL relations are more easily obtained at NIR wavelengths.

### 3. Period–Luminosity Relations

To establish the NIR PL relations, independent distance determinations are needed. First, we selected 20 of the 21 W UMa-type CBs with *Hipparcos* parallaxes characterized by distance-modulus uncertainties of  $\epsilon_M < 0.25$  mag (Rucinski 2006). The remaining system, TY Men, was excluded, since its light curve shows obvious unequal maxima, a signature of the O’Connell effect. Second, we collected a total of 6090 CBs with  $10 \leq V \leq 14$  mag, including 1131 and 5374 CBs from the General Catalog of Variable Stars (GCVS) and the ASAS Catalog of Variable Stars, respectively. In addition, we used the latest version of the DAML02 OC catalog (Dias et al. 2002, version 2016 January), which contains 2167 OCs.

Next, we considered individual publications focusing on CBs in a number of OCs, including NGC 188 (Zhang et al. 2004), NGC 1245 (Pepper & Burke 2006), NGC 2099 (Kang et al. 2007), NGC 2126 (Liu et al 2009), NGC 2158 (Mochejska et al. 2004), NGC 2204 (Rozyczka et al. 2007), NGC 2243 (Kaluzny et al. 2006), NGC 2301 (Kim et al. 2001), NGC 2539 (Choo et al. 2003), NGC 2682 (Yakut et al. 2009), NGC 5381 (Pietrzynski et al 1997), NGC 6253 (De Marchi et al. 2010), NGC 6259 (Ciechanowska et al. 2006), NGC 6705 (Koo et al. 2007), NGC 6791 (De Marchi et al. 2007), NGC 6819 (Street et al. 2002), NGC 6866 (Molenda-Żakowicz et al. 2009), NGC 6939 (Maciejewski et al. 2008), NGC 7044 (Kopacki et al. 2008), NGC 7142 (Sandquist et al. 2011), NGC 7789 (Mochejska & Molenda-Żakowicz09 Ka 1999), Berkeley 39 (Mazur et al. 1999), Collinder 261 (Mazur et al. 1995), and Melotte 66 (Zloczewski et al. 2007). These OC CBs contribute mostly to the faint end ( $V > 14$  mag) of the CB luminosity function.



To obtain a sample of high-probability OC CBs and reduce foreground/background contamination, we applied three selection criteria (Chen et al. 2015): (i) the CB of interest must be located inside the core radius of its host OC (Dias et al. 2002; Kharchenko et al. 2013, 2016); (ii) the CB’s proper motion must be located within the  $2\sigma$  distribution of that of its host OC; and (iii) the CB’s age,  $t$ , must be comparable to that of its host OC, where one typically adopts  $\Delta \log(t \text{ yr}^{-1}) < 0.3$  (e.g., Anderson et al. 2013). We adopted proper motions from the Fourth US Naval Observatory CCD Astrograph Catalog (UCAC4; Zacharias et al. 2013), complemented with measurements taken from the PPMXL Catalog (Roeser et al. 2010). Proper-motion selection is highly efficient in removing foreground CBs.

The evolution of CBs can roughly be divided into the detached, semi-detached, and contact phases. The mechanism that drives this evolution is thought to include Kozai cycles, accompanied by tidal friction (KCTF) and AML (Stępień 2006; Yıldız & Doğan 2013). Tokovinin et al. (2006) found that 96% of field binaries with orbital periods  $P < 3$  days include a third component. This third component tends to have a high inclination and can shorten the binary’s orbital period through KCTF. The associated timescale is very short, approximately 50 Myr (Eggleton & Kiseleva-Eggleton 2006). This mechanism becomes ineffective when the orbital period becomes shorter than approximately two days (Eggleton & Kiseleva-Eggleton 2006). Fabrycky & Tremaine (2007) also found that the KCTF process dominates binaries with periods  $2.0 < P < 3.0$  days. When the orbital period drops to less than 2 days, AML become effective. AML through magnetic winds is also called ‘magnetic braking;’ its timescale is longer than 1 Gyr. Therefore, only the AML timescale is considered here. The timescale governing the detached phase is almost the same as the time spent on the main sequence, which is determined by the initial mass of the primary component. The modern scenario that CBs are formed through AML can explain many observations, including:

1. CBs are preferentially found in intermediate-age or old OCs – e.g., NGC 188: 5 Gyr (Chen et al. 2016); Berkeley 39: 6 Gyr (Mazur et al. 1999); Collinder 261: 6 Gyr (Mazur et al. 1995) – and they are very rare in young,  $\sim 1$  Gyr-old OCs. Pre-CB counterparts (semi-detached and detached binaries) are found in young OCs (Rucinski 1998, 2000).
2. the density of CBs is 0.2% in the Galactic bulge and the solar neighborhood, but it decreases to 0.1% in the Galactic disk (Rucinski 2006). In relatively young environments, the fraction of CBs is low, while in old(er) environments this proportion increases. This means that the CB formation timescale is very long, comparable to the AML and nuclear-evolution timescales.
3. the CBs’ short-period limit. Rucinski (2007) used the ASAS catalog to conclude that

the short-period limit of CBs is 0.22 days. There may be a number of reasons for the appearance of such a limit: (i) CBs with effective temperatures below the full-convection point are dynamically unstable (Rucinski 1992); (ii) the formation timescale for short-period CBs is longer than the long AML timescale (Stępień 2006); and/or (iii) mass transfer in low-mass CBs is unstable and these CBs can only exist for very short periods (Jiang et al. 2012). However, following Rucinski (2007)’s publication, 367 ultra-short-period binaries, with periods of less than 0.22 days, have been found in the Catalina survey (Drake et al. 2014). This survey focuses on sources located away from the Galactic disk. Upon application of our PL relations (see below) to 202 ultra-short-period CBs with Sloan Digital Sky Survey colors, we find that 200 are in located the thick disk or halo, with only two residing in the Galactic thin disk. In addition, in the Galactic bulge the ultra-short-period limit to the CB distribution is around 0.19 days (Soszyński et al. 2015). Many shorter-period CBs are found in very old environments. This suggests that the long AML timescale may be the main reason for the short-period limit of CBs, since only this mechanism is directly related to the evolutionary timescale. We also speculate that the formation timescale of ultra-short-period (0.19 days) CBs may be close to the Hubble time.

4. the ultra-short period of detached binaries is around 0.09 days, which is significantly shorter than that for CBs (0.19 days) (Soszyński et al. 2015). Detached binaries are less evolved, whereas at least one component of CBs has evolved quite significantly (all hydrogen has been converted into helium in the stellar core). Ultra-short-period binaries are composed of two low-mass components; low-mass stars are characterized by longer nuclear-evolution timescales. This suggests that CB formation is limited by the long timescales of both nuclear evolution and AML.
5. the period–age relation of CBs and semi-detached binaries (Bukowiecki et al. 2012). Although period–age relations are not reliable for single CBs, a mean age–period relation (pertaining to a given cluster) may apply. If so, short periods are equivalent to lower luminosities (lower masses) and older ages.

OCs represent, to first approximation, single stellar populations. This means that all stellar members have the same age. The pre-CB evolutionary timescale must be shorter than their host open cluster’s age ( $t_{\text{cb}} < t_{\text{cl}}$ ) in order for these binaries to become CBs. This suggests that high-mass eclipsing binaries can evolve into CBs on short timescales. We obtain the limiting mass,  $M_{1,\text{limit}}$ , of the initial primary components from the limiting evolutionary timescale,  $t_{\text{cb}} = t_{\text{cl}}$ . Yıldız & Doğan (2013) have derived an expression for  $t_{\text{cb}}$

based on stellar evolution models, i.e.,

$$t_{\text{cb}} = \frac{10}{(M/M_{\odot})^{4.05}} \times \left( 5.60 \cdot 10^{-3} \left( \frac{M}{M_{\odot}} + 3.993 \right)^{3.16} + 0.042 \right) \quad (4)$$

The pre-CB counterparts satisfying  $m_{1,i} > m_{1,\text{limit}}$  can evolve into OC CBs. Based on this  $m_{1,\text{limit}}$  and different  $m_{2,i}$  values, we can estimate the lower limit to the current masses and luminosities of our sample CBs. CBs with luminosities below this limiting luminosity are likely background stars. This (conservative) age-selection criterion (see Fig. 1) is based on 100 well-studied CBs from Yıldız & Doğan (2013). Age selection is very effective in excluding background CBs. We checked whether the resulting PL relations would exhibit reduced scatter if we adopted tighter age constraints, but we did not find any difference. Among our sample OC CBs, two are characterized by  $0.2 \leq \Delta \log(t \text{ yr}^{-1}) < 0.3$  and three have  $0.1 \leq \Delta \log(t \text{ yr}^{-1}) < 0.2$ . However, these five CBs are affected by large uncertainties and low weights in establishing the PL relations.

After application of all three selection criteria, 42 high-probability OC CBs remain. Next, we determined CB distances and reddening values based on their host clusters’ properties. We collected the most recent results for every OC (see Table 1) and checked our results using NIR data from the Two Micron All Sky Survey (2MASS), where available.<sup>2</sup> We used the main-sequence fitting technique based on the Padova isochrones (Girardi et al. 2000), applied to the proper-motion-selected cluster members to estimate the distances and reddening values (Chen et al. 2015).

## 4. Results

Our final CB sample consists of 42 OC CBs, four nearby moving-group CBs with well-determined distances, and 20 W UMa-type CBs with high-accuracy *Hipparcos* parallaxes: see Table 1. Since the scatter in the PL relations decreases from  $V$  to  $K_s$  (e.g., Madore & Freedman 1991), we focus on the NIR PL relations. To establish the latter, we need access to the maximum  $JHK_s$  luminosities. Since the light-curve shapes do not change significantly as a function of wavelength compared with, e.g., Cepheid variables (because

---

<sup>2</sup>This analysis was done for NGC 188 (Hills et al. 2015), NGC 2158 (Carraro et al. 2002), NGC 2184 (Kharchenko et al. 2016), NGC 2243 (Anthony-Twarog & Twarog 2005), NGC 2682 (Geller 2015), NGC 6705 (Santos et al. 2005), NGC 6791 (Carney et al. 2005), NGC 6819 (Balona et al. 2013), NGC 6939 (Andreuzzi et al. 2004), NGC 7044 (Sagar & Griffiths 1998), NGC 7142 (Straižys et al. 2014), NGC 7789 (Wu et al. 2007), Berkeley 39 (Bragaglia et al. 2012), and Collinder 261 (Gozzoli et al. 1996).

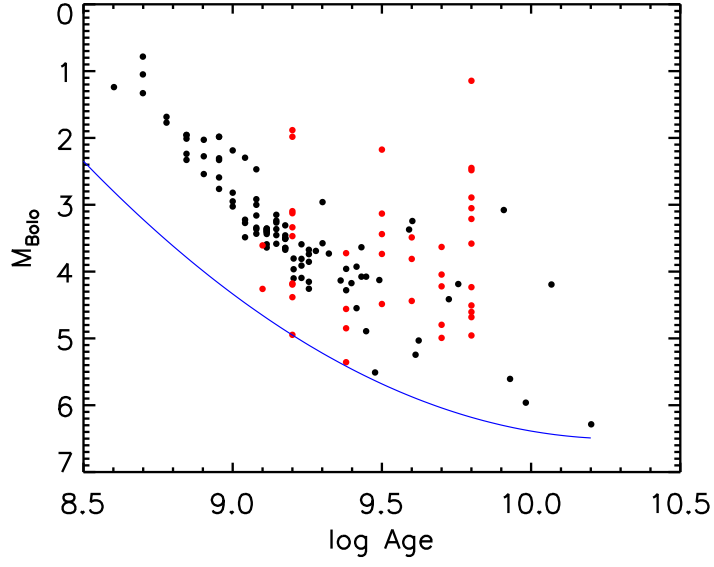


Fig. 1.— Age selection. Black dots: 100 well-studied CBs (Yıldız & Doğan 2013); solid line: lower limit to the ages of these CBs, characterized by  $\Delta \log(t \text{ yr}^{-1}) = 0.3$ ; red dots: final sample of 42 OC CBs.

the variations are caused by eclipses and the resulting BCs for the two binary components are negligible, given that they have similar temperatures), the maximum magnitude in a given band can be obtained by converting from single-epoch magnitudes to maximum luminosities using well-established light curves in the  $V$  band (taken from the literature). To reduce the effects of changes in the orbital period in our photometric conversions, for each CB we adopted the closest primary minimum epoch,  $T_0$ , to the observed 2MASS epoch. The maximum uncertainties of this conversion include 10% of total amplitude and 10% of phase uncertainty. The uncertainties in the absolute magnitudes (see Table 1) are a combination of the distance-modulus error, the photometric error, the extinction error, and these two conversion errors.

Table 1:: Calibration sample of 66 CBs.  $M_J(\varphi)$ ,  $M_H(\varphi)$ , and  $M_{K_s}(\varphi)$  are the absolute magnitudes at phase  $\varphi$ , which can be converted to maximum magnitudes using  $m_{\max} = m_\varphi - m_{\text{adj}}$ . DM (distance modulus),  $E(J - H)$ , and  $\log(t)$  are the best parameters for each OC.

| Contact Binary    | Period<br>(day) | $M_J(\varphi)$<br>(mag) | $M_H(\varphi)$<br>(mag) | $M_{K_s}(\varphi)$<br>(mag) | Phase ( $\varphi$ ) | $m_{\text{adj}}$<br>(mag) | OC            | DM<br>(mag) | $E(J - H)$<br>(mag) | $\log(t)$<br>[year] |
|-------------------|-----------------|-------------------------|-------------------------|-----------------------------|---------------------|---------------------------|---------------|-------------|---------------------|---------------------|
| V782 Cep          | 0.3583          | 3.145(161)              | 2.784(159)              | 2.661(164)                  | 0.83                | 0.05(01)                  | NGC 188       | 11.29(10)   | 0.03(01)            | 9.7                 |
| ep cep            | 0.2897          | 3.882(200)              | 3.443(225)              | 3.205(241)                  | 0.94                | 0.35(04)                  | NGC 188       | 11.29(10)   | 0.03(01)            | 9.7                 |
| eq cep            | 0.3070          | 4.013(210)              | 3.489(241)              | 3.372(255)                  | 0.10                | 0.40(04)                  | NGC 188       | 11.29(10)   | 0.03(01)            | 9.7                 |
| V370 Cep          | 0.3304          | 3.164(177)              | 2.879(178)              | 2.793(182)                  | 0.62                | 0.08(01)                  | NGC 188       | 11.29(10)   | 0.03(01)            | 9.7                 |
| es cep            | 0.3425          | 2.770(157)              | 2.521(512)              | 2.292(508)                  | 0.27                | 0.01(01)                  | NGC 188       | 11.29(10)   | 0.03(01)            | 9.7                 |
| AH CNC            | 0.3605          | 2.813(148)              | 2.571(146)              | 2.525(144)                  | 0.89                | 0.20(02)                  | NGC 2682      | 9.55 (10)   | 0.01(00)            | 9.5                 |
| EV CNC            | 0.4414          | 2.225(133)              | 1.935(126)              | 1.891(125)                  | 0.16                | 0.04(01)                  | NGC 2682      | 9.55 (10)   | 0.01(00)            | 9.5                 |
| HS CNC            | 0.3597          | 2.844(139)              | 2.535(136)              | 2.508(133)                  | 0.97                | 0.10(01)                  | NGC 2682      | 9.55 (10)   | 0.01(00)            | 9.5                 |
| NU CMa            | 0.2853          | 3.244(274)              | 2.795(283)              | 2.382(519)                  | 0.92                | 0.14(01)                  | NGC 2243      | 13.15(10)   | 0.02(01)            | 9.2                 |
| NW CMa            | 0.3565          | 2.681(196)              | 2.460(233)              | 2.118(284)                  | 0.61                | 0.14(01)                  | NGC 2243      | 13.15(10)   | 0.02(01)            | 9.2                 |
| V521 Lyr          | 0.3257          | 3.052(233)              | 2.938(292)              | 2.448(514)                  | 0.33                | 0.04(01)                  | NGC 6791      | 13.09(10)   | 0.04(01)            | 9.6                 |
| V513 Lyr          | 0.3917          | 2.783(207)              | 2.445(234)              | 2.377(515)                  | 0.20                | 0.05(01)                  | NGC 6791      | 13.09(10)   | 0.04(01)            | 9.6                 |
| J19203636+3739567 | 0.3664          | 3.269(252)              | 2.752(292)              | 2.467(325)                  | 0.44                | 0.20(02)                  | NGC 6791      | 13.09(10)   | 0.04(01)            | 9.6                 |
| V2388 Cyg         | 0.3660          | 2.805(230)              | 2.524(225)              | 2.429(243)                  | 0.33                | 0.03(01)                  | NGC 6819      | 11.87(14)   | 0.05(01)            | 9.4                 |
| V2396 Cyg         | 0.2932          | 3.542(245)              | 3.131(248)              | 2.910(294)                  | 0.95                | 0.20(02)                  | NGC 6819      | 11.87(14)   | 0.05(01)            | 9.4                 |
| V2393 Cyg         | 0.3032          | 3.592(257)              | 3.042(576)              | 2.597(568)                  | 0.05                | 0.15(02)                  | NGC 6819      | 11.87(14)   | 0.05(01)            | 9.4                 |
| V2394 Cyg         | 0.2562          | 4.052(256)              | 3.504(260)              | 3.439(563)                  | 0.66                | 0.10(01)                  | NGC 6819      | 11.87(14)   | 0.05(01)            | 9.4                 |
| NGC 6939 MGN V20  | 0.2951          | 3.747(281)              | 3.439(278)              | 3.232(289)                  | 0.99                | 0.50(05)                  | NGC 6939      | 11.41(10)   | 0.11(03)            | 9.1                 |
| NGC 6939 MGN V6   | 0.3599          | 2.536(203)              | 2.191(173)              | 2.052(175)                  | 0.18                | 0.02(01)                  | NGC 6939      | 11.41(10)   | 0.11(03)            | 9.1                 |
| KDK2008 v5        | 0.6150          | 1.576(503)              | 1.411(450)              | 1.170(432)                  |                     | 0.23(12)                  | NGC 7044      | 12.47(20)   | 0.20(06)            | 9.2                 |
| KDK2008 v6        | 0.6547          | 1.228(451)              | 1.011(393)              | 0.994(374)                  |                     | 0.13(07)                  | NGC 7044      | 12.47(20)   | 0.20(06)            | 9.2                 |
| KDK2008 v3        | 0.4606          | 2.261(505)              | 1.924(462)              | 1.866(472)                  |                     | 0.21(11)                  | NGC 7044      | 12.47(20)   | 0.20(06)            | 9.2                 |
| NGC 7789 KP V7    | 0.3375          | 3.146(309)              | 2.771(292)              | 2.661(299)                  | 0.49                | 0.12(01)                  | NGC 7789      | 11.42(20)   | 0.07(02)            | 9.2                 |
| V875 Cas          | 0.3063          | 3.430(337)              | 3.064(336)              | 2.959(341)                  | 0.15                | 0.37(04)                  | NGC 7789      | 11.42(20)   | 0.07(02)            | 9.2                 |
| J18510018–0614494 | 0.8696          | 0.569(331)              | 0.474(318)              | 0.493(558)                  | 0.33                | 0.05(03)                  | NGC 6705      | 11.33(20)   | 0.14(02)            | 8.4                 |
| J21451515+6549242 | 0.5808          | 1.564(220)              | 1.384(193)              | 1.319(171)                  | 0.94                | 0.07(01)                  | NGC 7142      | 11.98(10)   | 0.12(03)            | 9.5                 |
| J21442843+6546365 | 0.3302          | 3.370(215)              | 2.730(192)              | 2.736(175)                  | 0.00                | 0.36(01)                  | NGC 7142      | 11.98(10)   | 0.12(03)            | 9.5                 |
| J06071751+2404455 | 0.3555          | 2.608(274)              | 2.459(264)              | 2.385(281)                  |                     | 0.10(04)                  | NGC 2158      | 13.06(10)   | 0.13(03)            | 9.2                 |
| J06074059+2405035 | 0.3635          | 2.704(420)              | 2.399(387)              | 2.100(435)                  |                     | 0.24(05)                  | NGC 2158      | 13.06(20)   | 0.13(03)            | 9.2                 |
| V705 Mon          | 0.3810          | 2.560(465)              | 2.225(390)              | 2.551(444)                  | 0.87                | 0.05(09)                  | Berkeley 39   | 12.92(20)   | 0.03(03)            | 9.8                 |
| V711 Mon          | 0.3063          | 3.338(298)              | 2.653(316)              | 2.645(426)                  | 0.08                | 0.15(01)                  | Berkeley 39   | 12.92(20)   | 0.03(01)            | 9.8                 |
| V712 Mon          | 0.2844          | 3.364(352)              | 2.978(350)              | 3.329(621)                  | 0.30                | 0.03(01)                  | Berkeley 39   | 12.92(20)   | 0.03(01)            | 9.8                 |
| V704 Mon          | 0.2780          | 3.949(340)              | 2.933(387)              | 2.263(616)                  | 0.12                | 0.30(01)                  | Berkeley 39   | 12.92(20)   | 0.03(01)            | 9.8                 |
| V706 Mon          | 0.4865          | 2.004(433)              | 1.680(384)              | 1.922(628)                  | 0.56                | 0.16(02)                  | Berkeley 39   | 12.92(20)   | 0.03(01)            | 9.8                 |
| V701 Mon          | 0.5419          | 1.848(287)              | 1.661(314)              | 1.623(364)                  | 0.64                | 0.10(02)                  | Berkeley 39   | 12.92(20)   | 0.03(01)            | 9.8                 |
| V938 Mon          | 0.6820          | 1.023(278)              | 0.966(286)              | 0.802(324)                  | 0.63                | 0.16(01)                  | Berkeley 39   | 12.92(20)   | 0.03(01)            | 9.8                 |
| J23571065+5633268 | 0.2790          | 3.644(279)              | 3.142(281)              | 3.284(272)                  |                     | 0.05(01)                  | NGC 7789      | 11.42(20)   | 0.07(01)            | 9.2                 |
| IR Mus            | 0.3158          | 3.768(357)              | 3.440(400)              | 2.355(598)                  | 0.64                | 0.22(02)                  | Collinder 261 | 12.09(15)   | 0.08(03)            | 9.8                 |
| HM Mus            | 0.3431          | 3.523(346)              | 3.216(348)              | 2.904(606)                  | 0.13                | 0.30(03)                  | Collinder 261 | 12.09(15)   | 0.08(03)            | 9.8                 |
| HU Mus            | 0.5190          | 1.902(259)              | 1.722(241)              | 1.598(238)                  | 0.47                | 0.10(01)                  | Collinder 261 | 12.09(15)   | 0.08(03)            | 9.8                 |
| HZ Mus            | 0.4295          | 2.255(275)              | 2.034(242)              | 1.980(256)                  | 0.74                | 0.00(01)                  | Collinder 261 | 12.09(15)   | 0.08(03)            | 9.8                 |
| IO Mus            | 0.4009          | 2.480(300)              | 2.172(318)              | 2.113(299)                  | 0.03                | 0.28(03)                  | Collinder 261 | 12.09(15)   | 0.08(03)            | 9.8                 |
| ASAS061214–0347.4 | 0.3637          | 2.871(204)              | 2.581(197)              | 2.579(192)                  | 0.20                | 0.06(01)                  | NGC 2184      | 8.96 (15)   | 0.03(01)            | 8.7                 |
| ASAS081347–4034.2 | 0.5831          | 1.719(266)              | 1.692(255)              | 1.653(243)                  | 0.07                | 0.14(01)                  | Ruprecht 56   | 8.15 (20)   | 0.04(01)            | 8.8                 |
| TX Cnc            | 0.3829          | 2.867(147)              | 2.591(151)              | 2.528(141)                  | 0.10                | 0.20(02)                  | praesepe      | 6.16 (10)   | 0.01(00)            | 8.9                 |
| QX And            | 0.4122          | 2.175(130)              | 2.017(128)              | 1.961(125)                  | 0.16                | 0.03(01)                  | NGC 752       | 8.19 (10)   | 0.01(00)            | 9.2                 |
| VW Cep            | 0.2783          | 3.759(123)              | 3.222(102)              | 3.109(090)                  | 0.01                | 0.42(04)                  |               |             |                     |                     |
| OU Ser            | 0.2968          | 3.294(124)              | 3.030(144)              | 2.918(120)                  | 0.14                | 0.05(01)                  |               |             |                     |                     |
| SX Crv            | 0.3166          | 3.122(270)              | 2.855(284)              | 2.780(256)                  | 0.37                | 0.03(01)                  |               |             |                     |                     |

|          |        |            |            |            |      |          |
|----------|--------|------------|------------|------------|------|----------|
| YY Eri   | 0.3215 | 3.112(244) | 2.775(251) | 2.669(238) | 0.14 | 0.12(01) |
| W UMa    | 0.3336 | 2.935(204) | 2.585(209) | 2.546(192) | 0.32 | 0.04(01) |
| GM Dra   | 0.3387 | 2.636(205) | 2.384(198) | 2.341(192) | 0.71 | 0.02(01) |
| V757 Cen | 0.3432 | 3.353(171) | 3.049(199) | 2.940(179) | 0.90 | 0.22(02) |
| V781 Tau | 0.3449 | 2.749(235) | 2.463(231) | 2.405(229) | 0.67 | 0.08(01) |
| GR Vir   | 0.3470 | 3.506(169) | 3.264(169) | 3.220(174) | 0.92 | 0.40(04) |
| AE Phe   | 0.3624 | 3.054(147) | 2.765(144) | 2.658(147) | 0.11 | 0.19(02) |
| YY CrB   | 0.3766 | 2.813(208) | 2.579(230) | 2.482(214) | 0.42 | 0.25(03) |
| V759 Cen | 0.3940 | 2.726(127) | 2.484(143) | 2.421(127) | 0.03 | 0.20(02) |
| EX Leo   | 0.4086 | 2.223(236) | 2.006(248) | 1.938(243) | 0.37 | 0.06(01) |
| V566 Oph | 0.4096 | 2.171(142) | 2.007(152) | 1.961(146) | 0.22 | 0.01(01) |
| AW UMa   | 0.4387 | 2.087(152) | 1.948(148) | 1.916(154) | 0.73 | 0.02(01) |
| CN Hyi   | 0.4561 | 1.922(102) | 1.716(115) | 1.638(103) | 0.75 | 0.00(01) |
| RR Cen   | 0.6057 | 1.799(186) | 1.686(206) | 1.608(183) | 0.46 | 0.35(04) |
| IS CMa   | 0.6170 | 1.571(137) | 1.420(140) | 1.349(136) | 0.15 | 0.15(02) |
| V535 Ara | 0.6293 | 1.649(277) | 1.500(294) | 1.479(276) | 0.51 | 0.49(05) |
| S Ant    | 0.6484 | 1.454(114) | 1.327(126) | 1.232(102) | 0.35 | 0.11(01) |

Based on the 66 CBs in our calibration sample we obtain

$$\begin{aligned}
 M_{J_{\max}}^{\text{late}} &= (-6.15 \pm 0.13) \log P + (-0.03 \pm 0.05), \sigma_J = 0.09, \log P < -0.25; \\
 M_{J_{\max}}^{\text{early}} &= (-5.04 \pm 0.13) \log P + (0.29 \pm 0.05), \sigma_J = 0.09, \log P > -0.25; \\
 M_{H_{\max}} &= (-5.22 \pm 0.12) \log P + (0.12 \pm 0.05), \sigma_H = 0.08; \\
 M_{K_{s,\max}} &= (-4.98 \pm 0.12) \log P + (0.13 \pm 0.04), \sigma_K = 0.08.
 \end{aligned} \tag{5}$$

These PL relations—shown in Fig. 2—are as accurate as the  $JHK_s$  PL relations for Cepheids based on OC distances (Chen et al. 2015), which means that CBs can indeed be statistically competitive distance tracers to old stellar populations.

RR Lyrae also trace  $\gtrsim 1$ –2 Gyr-old stellar populations. However, their density is much lower than that of CBs. For instance, in the magnitude-limited ASAS survey, the number of RR Lyrae with  $V < 14$  mag is 1450. This is only a quarter of the number of late-type CBs in our sample (5374) and similar to the numbers of both Cepheids (1182) and early-type CBs (1582). Some long-period Cepheids may not have been detected. However, RR Lyrae periods are in the range 0.2–1.0 days, i.e., similar to those of CBs.

The magnitudes of RR Lyrae range from  $K_s = -0.5$  mag to  $K_s = +0.5$  mag; CB magnitudes range from  $K_s = -0.6$  mag to  $K_s = 4$  mag (late-type CBs:  $1 \lesssim K_s \lesssim 4$  mag). Early-type CBs ( $-0.6 \leq K_s \leq 1.0$  mag) are as bright as RR Lyrae and their number is roughly the same. CBs have as advantage that they trace intermediate-age environments (4–6 Gyr), while RR Lyrae represent the first choice to determine distances to old environments (older than 10 Gyr), such as old globular clusters.

The  $J$ -band PL relation is only reliable for late (W UMa)-type CBs; a small correction is needed for early-type CBs (for  $\log P > -0.25$ ; Rucinski 2006). The adjustment in the  $H$  band is less than the uncertainty; no correction is needed in the  $K_s$  band. In optical bands,

the differences between both types of CBs are more obvious on account of the period–color relation. Rucinski (2006) treated CBs with periods  $\log P > -0.25$  as early-type CBs and excluded them from his derivation of the late-type CB PL relation. Compared with late-type CBs, thus far the early-type CB PL(C) relation has been poorly studied, since the number of early-type CBs with accurate distance estimates has been limited. The theory underlying the early-type CB PL relation is not well-established compared with that pertaining to late-type CBs. Based on their periods, we infer that the initial primary components of early-type CBs,  $m_{1,i}$ , have higher masses compared to their counterparts in late-type CBs. For early-type CBs, when both components fill their Roche lobes,  $m_1$  is still larger than  $m_2$ , while late-type CBs undergo a mass reversal that leads to  $m_1 < m_2$  when both components fill their Roche lobes. Early-type CB have longer periods and need shorter evolutionary timescales.

The period–color relation can help us quantify the accuracy when converting PLC to PL relations. Figure 3 shows the NIR period–color relations for our full sample of 6090 CBs, adjusted for extinction corresponding to  $A_V = (0.54 \pm 0.23) \text{ mag kpc}^{-1}$  (see Fig. 4). We derived the latter trend from a statistical analysis of all 445 OCs with ages greater than  $10^9$  yr in the DAML02 catalog. The extinction per kiloparsec distance was derived for every OC; average values could then be obtained directly. A  $1\sigma$  cut was applied to exclude OCs with unusually deviating extinction characteristics. Since it is hard to de-redden 6090 CBs one by one, this extinction correction was applied statistically since we care about correcting trends in the PL relation(s), not derivation of the real extinction affecting individual CBs. The  $A_J, A_H$ , and  $A_K$  extinction values were taken from Rieke & Lebofsky (1985). These corrections have little influence on the NIR magnitudes, but they are needed in the  $V$  band. The best-fitting period–color relations are

$$\begin{aligned} (J - K_s)_0 &= -1.19 \log P + (-0.16 \pm 0.02), \sigma_{JK_s} = 0.09, \\ (H - K_s)_0 &= -0.20 \log P + (-0.02 \pm 0.01), \sigma_{HK_s} = 0.03, \\ (V - K_s)_0 &= -4.14 \log P + (-0.36 \pm 0.08), \sigma_{VK_s} = 0.38, \end{aligned} \quad (6)$$

and

$$\begin{aligned} (J - K_s)_0 &= 0.03 \log P + (0.17 \pm 0.02), \sigma_{JK_s} = 0.07, \\ (H - K_s)_0 &= -0.00 \log P + (0.04 \pm 0.01), \sigma_{HK_s} = 0.04, \\ (V - K_s)_0 &= -0.04 \log P + (0.72 \pm 0.07), \sigma_{VK_s} = 0.38, \end{aligned} \quad (7)$$

for  $\log(P \text{ day}^{-1}) < -0.25$  (Eq. 6) and  $\log(P \text{ day}^{-1}) > -0.25$  (Eq. 7), respectively. These relations are almost independent of the PL relations of Eq. (5). A careful comparison shows that both sets of equations above are in good mutual agreement, although a correction to the early-type CB PL relation is required (as already discussed in the context of the PL relations). We show the curves resulting from application of modern, non-parametric regression techniques in Figs 3–5, which were obtained using the standard Matlab `ksrlin`



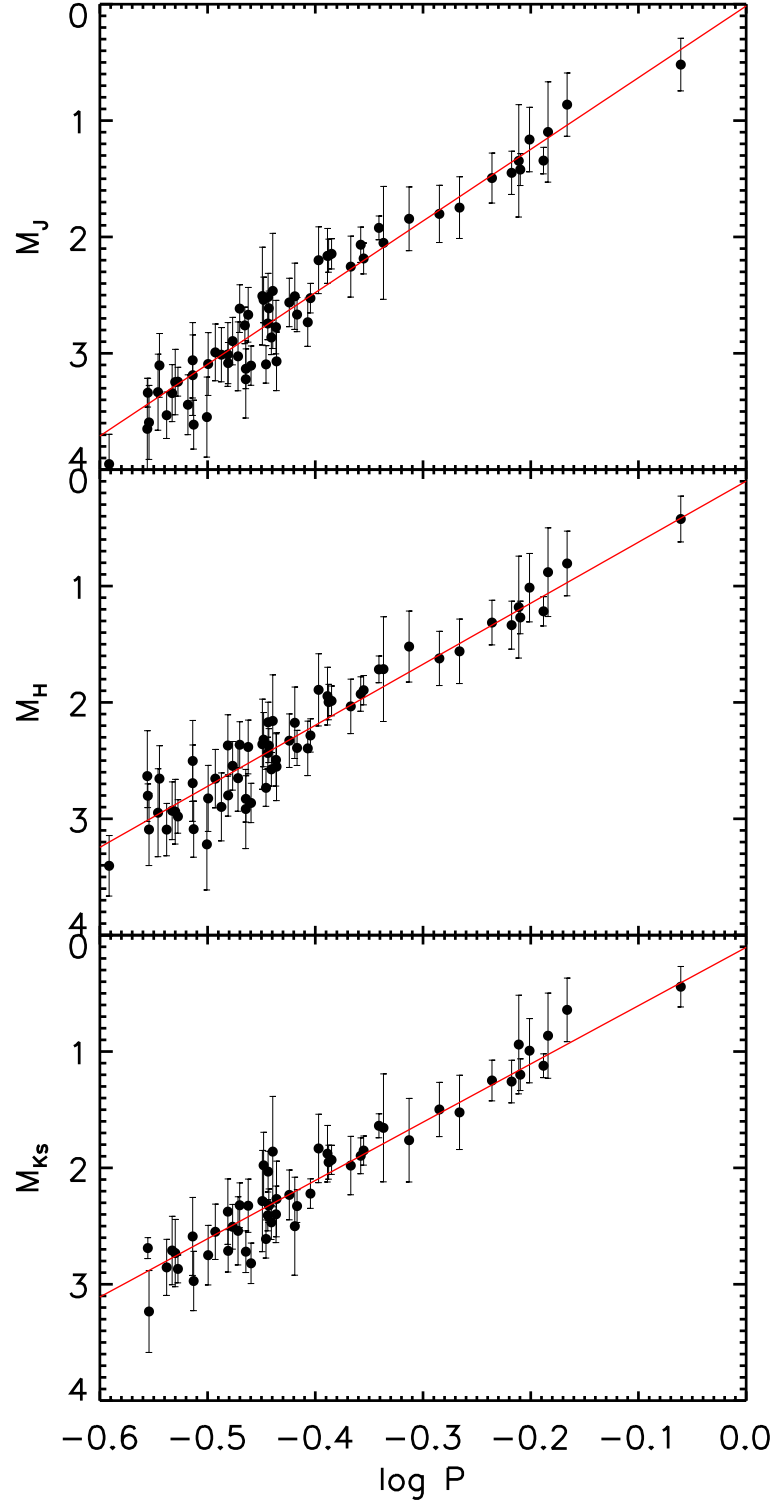


Fig. 2.—  $JHK_s$  PL relations determined based on our 66 calibration CBs.

and `ksr` local linear kernel smoothing regression functions. For Figs 3 and 5 we used the default conditions, while for Fig. 4 we used a bandwidth or smoothing parameter  $h = 200$ . This kind of approach is very useful when dealing with large- $N$  sample data without having to make ‘linear’ assumptions; it allows us to detect non-linear features. This technique was applied to ensure that our linear fit is sufficient to cover the full distribution of our data points. The green dotted lines (in all three figures) are based on local linear regression techniques, while the black dash-dotted lines are based on smooth regression. These curves are comparable to our linear fits, considering the uncertainties, especially in the  $H - K_s$  diagram. This implies that Eq. 6 are reliable period–color relations.

From our newly established  $JHK_s$  PL relations, the  $V$ -band PL relation can be derived using the NIR distances. We adopted  $V_{\max}$  values from different literature sources, so large uncertainties caused by calibration inhomogeneities are inevitable for individual CBs. However, use of such a large sample makes their combination statistically more reliable by averaging out calibration differences, provided that the latter are not dominated by unrecognized systematic errors. The resulting  $V$ -band PL relation (see Fig. 5) is

$$\begin{aligned} M_{V_{\max}} &= (-9.15 \pm 0.12) \log P + (-0.23 \pm 0.05), \sigma_V = 0.30 (\log P < -0.25), \\ M_{V_{\max}} &= (-4.95 \pm 0.13) \log P + (0.85 \pm 0.02), \sigma_V = 0.35 (\log P > -0.25). \end{aligned} \quad (8)$$

## 5. Discussion

### 5.1. Assumptions and error budget

In Table 1 and Section 4, we explained how we obtained the maximum NIR magnitudes for all of our 66 calibration CBs. In this section, we discuss the underlying assumptions we had to make and the overall error budget. One important assumption is that the NIR reddening law is universal. Another major assumption is that the differential reddening across the face of each cluster is small, so that for a given OC CB we can adopt its host cluster’s reddening. Since these OCs and CBs are affected by only little extinction—for most,  $E(J - H) < 0.1$  mag—the anticipated influence imposed by these effects can indeed be ignored. A third main assumption we made is that most CBs are only affected by small period changes, if any. We adopted the closest primary minimum epoch,  $T_0$ , to the observed 2MASS epoch to avoid any effects caused by period changes. Our final key assumption is that the light-curve shapes do not change significantly as a function of wavelength. These latter two assumptions will contribute 10% uncertainties to both the total amplitude and the phase uncertainty for a given CB. The overall error includes the uncertainty associated with the distance modulus,  $\sigma_{\text{DM}}$ , obtained using either parallaxes or the OC main-sequence

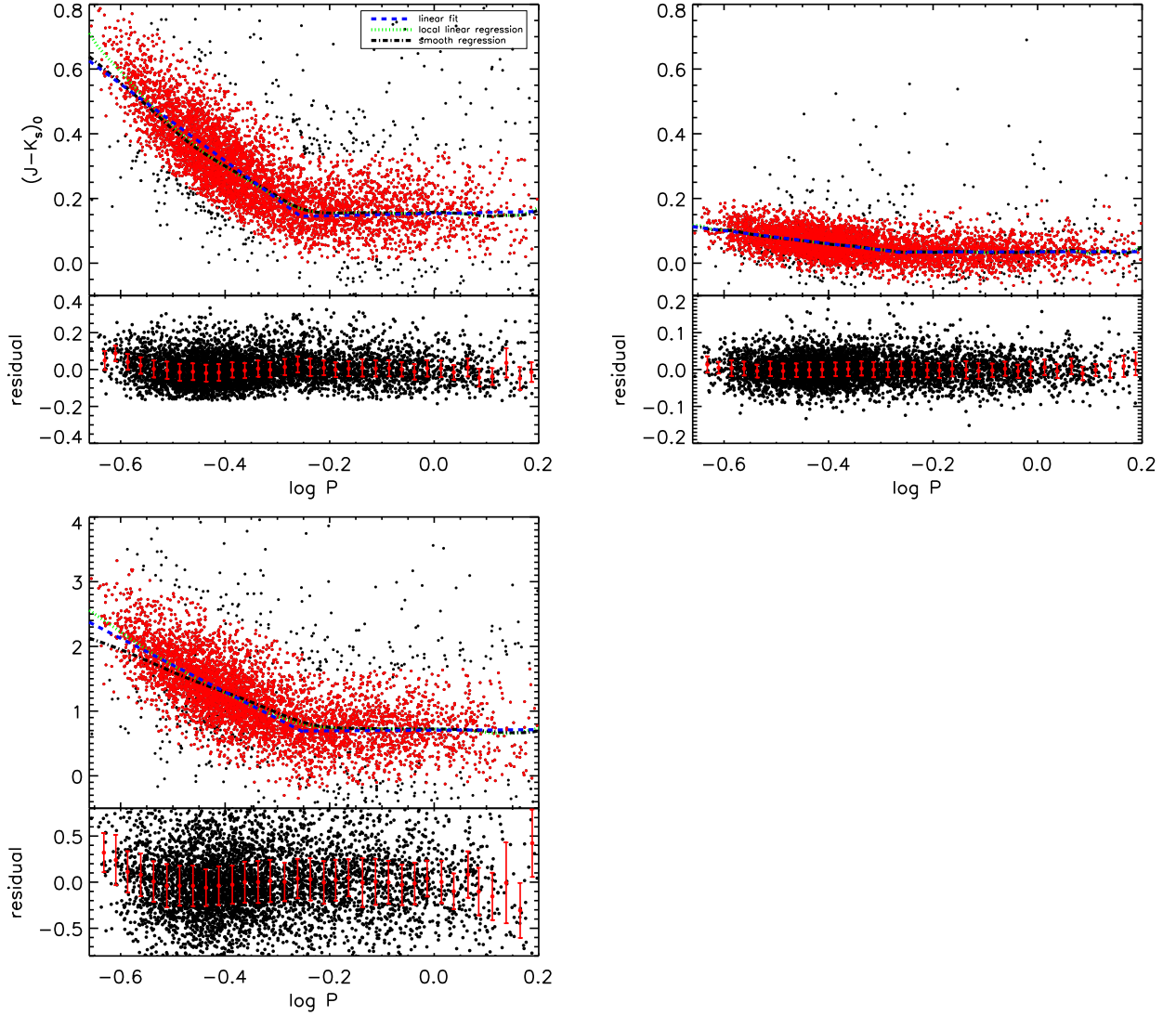


Fig. 3.— Period–color relations for our full sample of 6090 CBs. Early- and late-type CBs each follow different period–color relations. The best fits are shown as solid lines. Red dots: CBs located within the  $3\sigma$  distributions. Black dots: CBs with poor-quality photometry, affected by complicated differential extinction, or objects that are not genuine CBs. The residuals are also shown for each relation. Green dotted lines are based on local linear regression, while black dash-dotted lines are based on smooth regression. Although the  $J - K_s$  and  $V - K_s$  diagrams may exhibit small trends at the short- and long-period extremes, these only cover a few tens of CBs and may not be real. Indeed, they also disappear in the less reddening-sensitive  $H - K_s$  diagram.

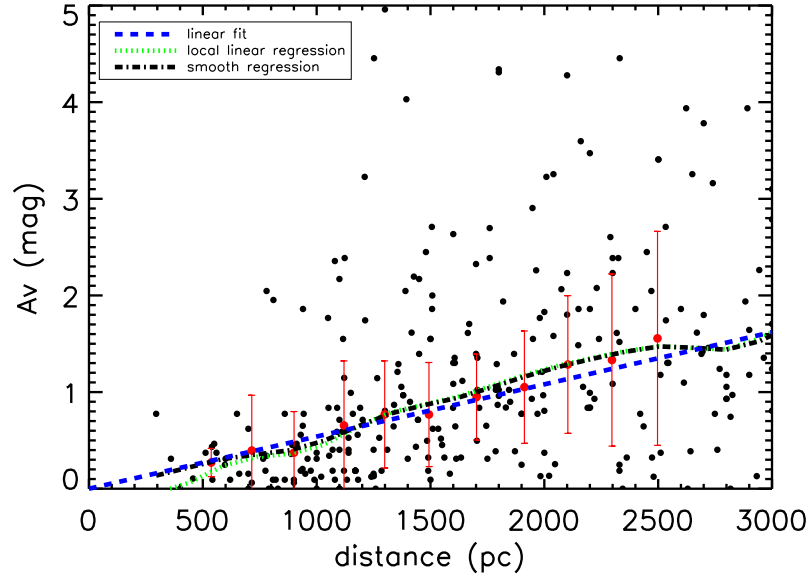


Fig. 4.—  $V$ -band extinction of 445 old OCs obtained from the DAML02 catalog (Dias et al. 2002). The blue circles are the average extinction values in each bin at distances from 400 pc to 2600 pc. The red dashed line is the statistical average extinction,  $A_V = 0.54 \pm 0.23$  mag  $\text{kpc}^{-1}$ , based on all black points. The green dotted and black dash-dotted lines are based on local linear regression and smooth regression, respectively.

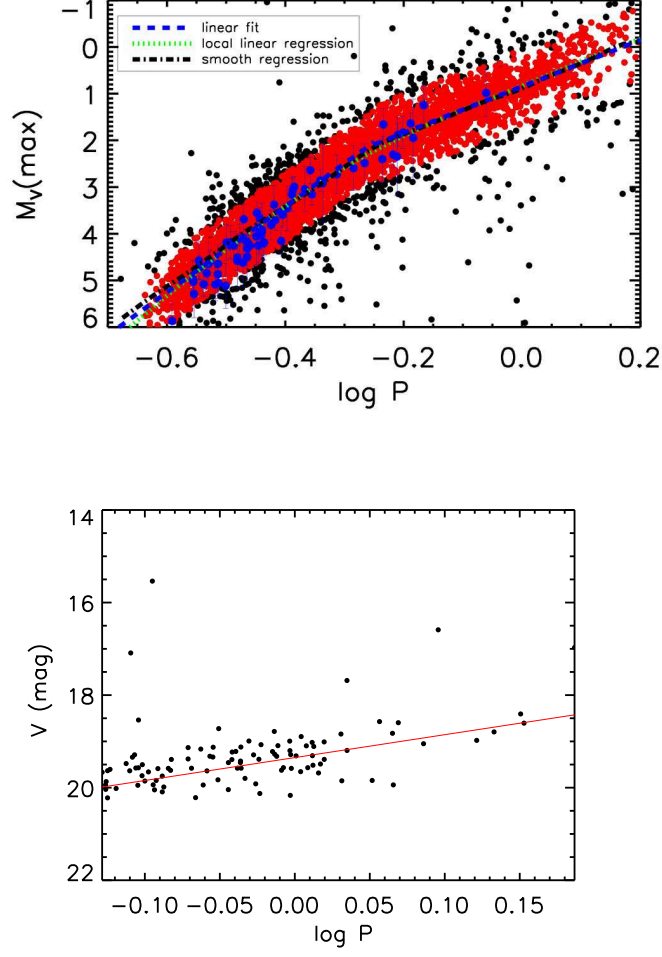


Fig. 5.—  $V$ -band PL relations for (top) our full sample of 6090 CBs (black dots) and (bottom) the LMC CBs. Top: the PL relations for early- and late-type CBs are determined separately for periods shorter and longer than  $\log(P \text{ day}^{-1}) = -0.25$ . Blue dots: our sample of 66 calibration objects. Bottom: the red solid line is the  $V$ -band PL relation for Galactic CBs, Eq. (8).

fitting method, the photometric error,  $\sigma_{\text{pho}}$ , the extinction-correction error,  $\sigma_{\text{ext}}$ , and the uncertainty caused by converting single-epoch magnitudes to maximum magnitudes,  $\sigma_{\text{conv}}$ . The maximum overall error  $\sigma = \sigma_{\text{DM}} + \sigma_{\text{pho}} + R_{\text{filter}}\sigma_{\text{ext}} + \sigma_{\text{conv}}$ , where  $R_{\text{filter}}$  is the total to selective extinction (i.e., the extinction law) for a given filter. These uncertainties are reported in Table 1.

## 5.2. Previous PLC or PL relations

Rucinski (1994) derived a widely used PLC relation for late-type CBs. Subsequently, Rucinski (2006) tried to derive a PL relation based on 21 nearby, late-type CBs with accurate *Hipparcos* parallaxes; within the significant uncertainties, only 11 of his 21 objects followed the resulting PL relation,  $V = (12.0 \pm 2.0) \log P + (-1.5 \pm 0.8)$ . Our PL relation is much shallower. This difference can be easily understood. Rucinski (1994)’s PL relation was based on only 10 objects, a sample where the CB with the shortest period (VW Cep;  $\log P = -0.55$ ) determined the slope. In our period–color relation (Fig. 5), the slope is constrained by a large number of intermediate-period CBs ( $-0.5 < \log P < -0.3$ , in days) and not by their short-period ( $\log P < -0.55$ ) counterparts. In addition, both short- and long-period ( $\log P > 0.1$ ) CBs are affected by sampling incompleteness, which is caused by the obvious cut-offs at  $\log P = -0.6$  and  $\log P = 0.2$ , respectively. The short-period cut-off is driven by the long formation timescale of faint CBs (longer than the age of the Milky Way), while long-period CBs easily lose their angular momentum because of the convective nature of the stellar surfaces. The latter determines the upper limit to the initial stellar mass and, hence, the upper limit to the period. To correct the Rucinski (2006) PL relation for potential selection effects, we applied weights to his data as a function of orbital period, using the magnitude uncertainty. We plotted the orbital-period distribution in 0.01 dex bins, and we calculated the probability  $\xi_i$  in each bin. If  $n$  of Rucinski (2006)’s CBs are located in a given bin, the probability weights of these CBs are  $\frac{\xi_i}{n}$ . We next consider the uncertainties,  $\sigma_M$ , in the absolute magnitudes of these CBs. The final weight is  $\frac{\xi_i}{n\sigma_M^2}$ , for each CB. The revised PL relation based on the Rucinski (2006)’s data thus corrected is  $V = (-11.4 \pm 1.7) \log P + (-1.2 \pm 0.8)$  mag, which is indeed close to our result. If we exclude TY Men, the newly revised PL relation becomes  $V = (-10.5 \pm 2.2) \log P + (-0.9 \pm 1.0)$  mag, which is even closer to our result.

### 5.3. NIR PL relation accuracy

Most recent studies using Cepheids as distance tracers are based on NIR PL relations. They are more accurate and significantly less sensitive to extinction and metallicity variations than  $V$ -band PL relations. In this paper, we derived the first PL relations for bright, early-type CBs, which allows the application of CBs to trace features at greater distances compared with the use of the late-type CB PL relation. This study has thus made CBs a viable distance tracer pertaining to old environments. Combining the  $JHK_s$  PL relations, we derived the distances to our full sample of 6090 CBs. The resulting accuracy is high: 90% of our sample CBs have distance errors of less than 5%, and 95% have distance uncertainties of less than 10%. The remaining 5% may be CBs with poor-quality photometry, CBs affected by complicated differential extinction (or severe reddening), or objects that have been misidentified as CBs. The latter include small-amplitude RR Lyrae and ellipsoidal binaries.

We will now evaluate the accuracy in distance as determined by our NIR PL relations. By combining all three NIR PL relations, the statistical uncertainty will decrease to 0.05 mag. The systematic error includes the zero-point errors in the PL relations, the reddening error, the metallicity error, and the photometric uncertainties. Since our PL relation relies on the distances to our sample OCs and on the parallaxes, zero-point errors were introduced by the method we used for distance determination. The distance-modulus uncertainties of the 17 sample OCs for which we obtained distances in this manner (see Table 1) are 0.1–0.2 mag and the average distance-modulus error associated with the 20 CBs in our sample for which we have access to *Hipparcos* parallaxes is 0.137 mag. The average of the combined sample of 18 distances is  $\sigma = 0.138$  mag and so the error in the zero-point is  $\frac{\sigma}{\sqrt{n}} = 0.032$  mag. As for the reddening uncertainty, the NIR reddening error is very small compared with those in optical bands, with  $A_J/A_V = 0.282$ ,  $A_H/A_V = 0.175$ ,  $A_K/A_V = 0.112$  (Rieke & Lebofsky 1985). More than half of our CBs are nearby CBs, and they have a reddening corresponding to  $E(B - V) < 0.08$  mag. Even if the  $R_V = 3.1$  reddening law would need to be adjusted by 25%, the NIR reddening error would still be less than 0.01 mag. Although the reddening may still contribute to the statistical error, it is not a significant contributor to the systematic error.

The metallicity error is caused by the different metallicities of the CBs used to derive the PL relation, which could potentially result in a PL relation that depends on metallicity. To evaluate this possibility, a relation between  $\Delta M$  and  $[\text{Fe}/\text{H}]$  must be established, where  $\Delta M$  is the deviation of the observed absolute magnitudes to the predicted absolute by PL relation. Fortunately, for 48 of our 66 calibration CBs we have access to direct metallicity information (Rucinski et al. 2013) or to metallicity measurements obtained for their host OCs (Dias et al. 2002). All of the latter metallicities were obtained from the latest available



literature sources. The NIR  $\Delta M$ –[Fe/H] relations are  $M_J = 0.29[\text{Fe}/\text{H}] \pm 0.14$  mag,  $M_H = 0.28[\text{Fe}/\text{H}] \pm 0.12$  mag, and  $M_{K_s} = 0.21[\text{Fe}/\text{H}] \pm 0.15$  mag (see Fig. 6). This means that if CBs with  $[Fe/H] = -1.0$  dex are used to derive the PL relations, a systematic uncertainty of at least 0.2 mag may be applicable. The average metallicity of the 48 CBs is  $\overline{[\text{Fe}/\text{H}]} = -0.041$  dex, so the systematic error introduced by metallicity differences is around  $\sigma = 0.01$  mag. The total systematic error is  $\sigma_{\text{sys}}^2 = \sigma_{\text{zp}}^2 + \sigma_{\text{ext}}^2 + \sigma_{\text{metal}}^2$ , i.e.,  $\sigma_{\text{sys}} = 0.03$  mag. As a result, the accuracy of using CBs as distance tracers is  $0.05$  (statistical)  $\pm 0.03$  (systematic) mag.

#### 5.4. distance to LMC

Graczyk et al. (2011) published a catalog of 26,121 eclipsing binary stars in the LMC, identified based on visual inspection of the Optical Gravitational Lensing Experiment III catalog. Their 1048 type-EC eclipsing binaries are CBs. In fact, based on their light curves, most are semi-detached binaries with unequal minima and other types of variable stars. They only included CBs with long periods ( $\log P > -0.2$ ). To select CBs that can be used as distance tracers, we adopted the period–color selection of Eq. (8) and Fig. 3. We derived a color cut at  $(V - I)_0 = (0.41 \pm 0.21)$  mag using the transformation equations of Bessell et al. (1998). We imposed a period selection of  $-0.13 < \log P < 0.2$ , where the upper limit is at the long-period end of the CB distribution and the lower limit is the magnitude limit for detecting LMC CBs. This led to a final sample of 102 LMC CBs, resulting in a distance modulus of  $(m - M_V)_0 = 18.41 \pm 0.20$  mag. This is first distance to the LMC that was determined based on CBs. It is fully consistent with the current best LMC distance modulus (de Grijs et al. 2014),  $(m - M)_0 = 18.49 \pm 0.09$  mag. Figure 5 shows that the LMC CBs follow the same PL relation as their counterparts in our Galaxy. Previous studies of large samples of eclipsing binary systems in the LMC (Muraveva et al. 2014; Pawlak 2016) did not find a clear PL relation, since they did not correct for the prevailing period–color relations.

### 6. Summary

We collected CBs in OCs and CBs with accurate *Hipparcos* parallaxes. Our full sample contains 6090 CBs from the GCVS and ASAS surveys, while the OC sample contains 2167 OCs. To exclude foreground and background CBs, (i) the CB of interest must be located inside the core radius of its host OC; (ii) the CB’s proper motion must be located within the  $2\sigma$  distribution of that of its host OC; and (iii) the CB’s age must be comparable to that of its host OC,  $\Delta \log(t \text{ yr}^{-1}) < 0.3$ . We thus selected 42 high-probability OC CBs. Combined

with four nearby moving-group CBs and 20 W UMa-type CBs with accurate *Hipparcos* parallaxes, a sample of 66 CBs is used to determine the  $JHK_s$  PL relations. The latter yield distances that are as accurate as those resulting from the  $JHK_s$  Cepheid PL relations ( $\sigma < 0.10$  mag).

NIR PL relations for early-type CBs are obtained for the first time. To check the reliability of our PL relations, the CB period–color relations are also investigated. These can be used to exclude unreliable CBs. We discuss the potential of CBs as distance tracers and find that they can determine distances to 5% uncertainty for 90% of the objects in our full sample. We also discuss the overall uncertainty associated with using CBs as distance tracers and we derive a value of  $\sigma = 0.05$  (statistical)  $\pm 0.03$  (systematic) mag. The 102 CBs in the LMC satisfying our period–color selection are used to determine an LMC distance modulus of  $(m - M_V)_0 = 18.41 \pm 0.20$  mag.

Since more than 30,000 CBs have been found in the GCVS, ASAS, OGLE III, and Catalina catalogs, and hundreds of additional CBs are reported on by individual studies every year, CBs can be important tracers to study the structure of our Galaxy. However, given the NIR relations determined here, more accurate NIR absolute magnitudes should be obtained for a large sample of CBs to make this aim a reality. Combined with information about their periods, physical parameters from light-curve solutions, and age information from the host clusters, the formation and evolution mechanisms of CBs could indeed be much better understood. *Gaia* will observe most known CBs; distances derived based on our PL relations can hence be used as a cross check of the *Gaia* parallaxes anticipated soon.

We thank acknowledge useful comments from an anonymous referee. We are grateful for research support from the National Natural Science Foundation of China through grants 11373010 and 11473037.

## REFERENCES

- Anderson R. I., Eyer L., Mowlavi N. 2013, MNRAS, 434, 2238
- Andreuzzi, G., Bragaglia, A., Tosi, M., & Marconi, G. 2004, MNRAS, 348, 297
- Anthony-Twarog, B. J., Atwell, J., & Twarog, B. A. 2005, AJ, 129, 872
- Balona, L. A., Medupe, T., Abedigamba, O. P., et al. 2013, MNRAS, 430, 3472
- Bessell, M. S., Castelli, F., & Plez, B. 1998, A&A, 333, 231

- Bragaglia, A., Gratton, R. G., Carretta, E., et al. 2012, *A&A*, 548, 122
- Bukowiecki, L., Maciejewski, G., Konorski, P., Errmann, R. 2012, *IBVS*, 6021, 1
- Carney, B. W., Lee, J.-W., & Dodson, B. 2005, *AJ*, 129, 656
- Carraro, G., Girardi, L., & Marigo, P. 2002, *MNRAS*, 332, 705
- Chen, X. D., de Grijs, R., & Deng, L. C. 2015, *MNRAS*, 446, 1268
- Chen, X. D., Deng, L. C., de Grijs, R., et al. 2016, *AJ*, in press (arXiv:1607.06152)
- Choo, K. J.; Kim, S.-L.; et al. 2003, *A&A*, 399, 99
- Ciechanowska, A., Pietrzynski, G., et al. 2006, *AcA*, 56, 219
- de Grijs, R., Wicker, J. E., & Bono, G. 2014, *AJ*, 147, 122
- De Marchi, F. Poretti, E., Montalto, M., et al. 2007, *A&A*, 471, 515
- De Marchi, F., Poretti, E., Montalto, M., et al. 2010, *A&A*, 509, A17
- Dias, W. S., Alessi, B. S., Moitinho, A., & Lépine, J. R. D. 2002, *A&A*, 389, 871
- Drake, A. J., Djorgovski, S. G., et al. 2014, *ApJ*, 790, 157
- Eggen, O. J. 1967, *MmRAS*, 70, 111
- Eggleton, P.P., & Kiseleva-Eggleton, L. 2006, *Ap&SS*, 304, 75
- Fabrycky, D., & Tremaine, S. 2007, *ApJ*, 669, 1298
- Geller, A. M., Latham, D. L., & Mathieu R. D. 2015, *AJ*, 150, 97
- Girardi, L., Bressan, A., Bertelli, G., & Chiosi, C. 2000, *A&AS*, 141, 371
- Gozzoli, E., Tosi, M., Marconi, G. & Bragaglia, A. 1996, *MNRAS*, 283, 66
- Graczyk, D., Soszyński, I., Poleski et al. 2011, *AcA*, 61, 103
- Hills, S., von Hippel, T., Courteau, S., & Geller, A. M. 2015, *AJ*, 149, 94
- Jiang, D. K., Han, Z. W. et al. 2012, *MNRAS*, 421, 2769
- Kaluzny, J., Krzeminski, W., Thompson, I. B., Stachowski, G. 2006, *AcA*, 56, 51
- Kang, Y. B., Kim, S.-L.; Rey, S.-C. et al. 2007, *PASP*, 119, 239

- Kharchenko, N. V., Piskunov, A. E., Schilbach, E., Röser, S., & Scholz, R.-D. 2013, *A&A*, 558, 53
- Kharchenko, N. V., Piskunov, A. E., Schilbach, E., Röser, S., & Scholz, R.-D., 2016, *A&A*, 585, 101
- Kim, S. -L., Chun, M. -Y., Park, B. -G., et al. 2001, *A&A*, 371, 571
- Koo, J.-R., Kim, S.-L., Rey, S.-C., et al. 2007, *PASP*, 119, 1233
- Kopacki, G., Drobek, D., et al. 2008, *AcA*, 58, 373
- Kuiper, G. P. 1941, *ApJ*, 93, 133
- Liu, S.-F., Wu, Z.-Y. et al. 2009, *RAA*, 9, 791
- Lucy, L. B. 1968, *ApJ*, 151, 1123
- Maciejewski, G., Georgiev, Ts., & Niedzielski, A. 2008, *AN*, 329, 387
- Madore, B. F., & Freedman, W. L. 1991, *PASP*, 103, 933
- Mazur, B., Krzeminski, W., & Kaluzny, J. 1995, *MNRAS*, 273, 59
- Mazur, B., Krzeminski, W., & Kaluzny, J. 1999, *AcA*, 49, 551
- Mochejska, B. J., & Kaluzny, J. 1999, *AcA*, 49, 351
- Mochejska, B. J., Stanek, K. Z., Sasselov, D. D., et al. 2004, *AJ*, 128, 312
- Molenda-Żakowicz, J., Kopacki, G., et al. 2009, *AcA*, 59, 193
- Muraveva, T., Clementini, G., Maceroni, C., et al. 2014, *MNRAS*, 443, 432
- Pawlak, M. 2016, *MNRAS*, 457, 4323
- Rieke, G. H., & Lebofsky, M. J. 1985, *ApJ*, 288, 618
- Röser, S., Demleitner, M., & Schilbach, E. 2010, *AJ*, 139, 2440
- Rozyczka, M., Kaluzny, J., et al. 2007, *AcA*, 57, 323
- Rucinski, S. M. 1992, *AJ*, 103, 960
- Rucinski, S. M. 1994, *PASP*, 106, 462
- Rucinski, S. M., & Duerbeck, H. W. 1997, *PASP*, 109, 1340

- Rucinski, S. M. 1998, *AJ*, 116, 2998.
- Rucinski, S. M. 2000, *AJ*, 120, 319.
- Rucinski, S. M. 2006, *MNRAS*, 368, 1319
- Rucinski, S. M. 2007, *MNRAS*, 382, 393
- Rucinski, S. M. Pribulla, T. Budaj, J. 2013, *AJ*, 146, 70
- Sagar, R., & Griffiths, W. K. 1998, *MNRAS*, 299, 1
- Sandquist, E. L., Serio, A. W., & Shetrone, M. 2011, *AJ*, 142, 194
- Santos, J. F. C. Jr., Bonatto, C., & Bica, E. 2005, *A&A*, 442, 201
- Stępień, K, 2006, *Acta Astron.*, 56, 199
- Straizys V., Maskoliunas M., Boyle R. P., et al. 2014, *MNRAS*, 437, 1628
- Street, R. A., et al. 2002, *MNRAS*, 330, 737
- Soszyński, I., Stępień, K., et al. 2015, *AcA*, 65, 39
- Pepper, J, Burke, C. J. 2006, *AJ*, 132, 1177
- Pietrzynski, G., Kubiak, M., Udalski, A., Szymanski, M. 1997, *AcA*, 47, 437
- Tokovinin, A., Thomas, S., Sterzik, M., Udry, S. 2006, *A&A*, 450, 681
- Wu, Z.-Y., Zhou, X., Ma, J., et al. 2007, *AJ*, 133, 2061
- Yıldız, M., & Doğan, T. 2013, *MNRAS*, 430, 2029
- Yıldız, M. 2014, *MNRAS*, 437, 185
- Yakut, K., Zima, W., Kalomeni, B., et al. 2009, *A&A*, 503, 165
- Zacharias, N., Finch, C. T., Girard, T. M., et al. 2013, *AJ*, 145, 44
- Zhang, X. B., Deng, L. C., Zhou, X., & Xin, Y. 2004, *MNRAS*, 355, 1369
- Złoczewski, K., Kaluzny, J., Krzeminski, W., Olech, A., & Thompson, I. B. 2007, *MNRAS*, 380, 1191

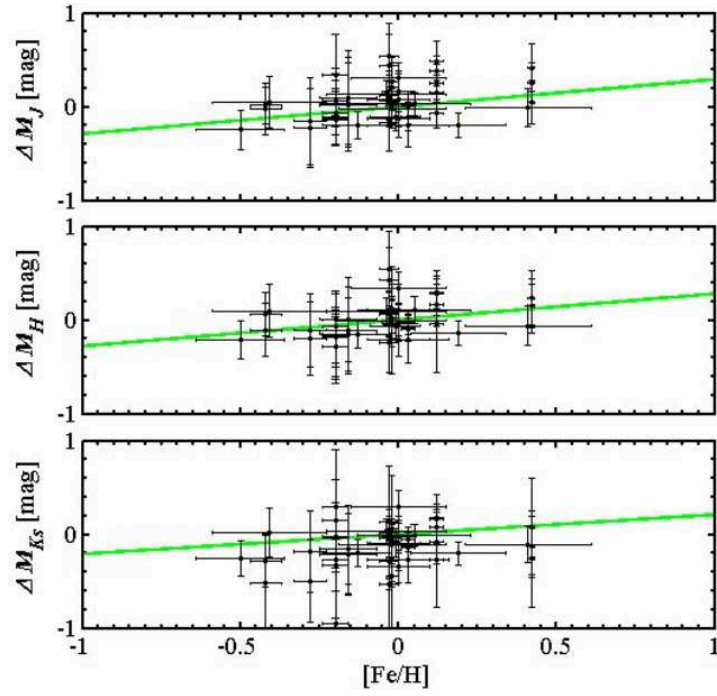


Fig. 6.— NIR PL relation magnitude residuals as a function of metallicity. The green solid lines are linear fits.